

Research Article

Open Access



# Fabrication of subnanometric Ni clusters over the Ni/SAPO-11 hydroisomerization catalyst

Yuchao Lyu<sup>1,\*</sup>, Lei Fan<sup>1,#</sup>, Yiming Gao<sup>1</sup>, Lianming Zhao<sup>2</sup>, Wenjing Zhang<sup>1</sup>, Furang Li<sup>1</sup>, Jianye Fu<sup>1</sup>, Xinmei Liu<sup>1,\*</sup>

<sup>1</sup>State Key Laboratory of Heavy Oil Processing, China University of Petroleum, Qingdao 266580, Shandong, China.

<sup>2</sup>College of Materials Science and Engineering, China University of Petroleum, Qingdao 266580, Shandong, China.

#Authors contributed equally.

\*Correspondence to: Dr. Yuchao Lyu, Dr. Xinmei Liu, State Key Laboratory of Heavy Oil Processing, China University of Petroleum, No.66, West Changjiang Road, Huangdao District, Qingdao 266580, Shandong, China. E-mail: yuchaolyu@upc.edu.cn; lxmei@upc.edu.cn

**How to cite this article:** Lyu, Y.; Fan, L.; Gao, Y.; Zhao, L.; Zhang, W.; Li, F.; Fu, J.; Liu, X. Fabrication of subnanometric Ni clusters over the Ni/SAPO-11 hydroisomerization catalyst. *Chem. Synth.* **2025**, *5*, 55. <https://dx.doi.org/10.20517/cs.2024.88>

**Received:** 19 Jul 2024 **First Decision:** 6 Sep 2024 **Revised:** 25 Sep 2024 **Accepted:** 10 Oct 2024 **Published:** 13 Jun 2025

**Academic Editor:** Yi Tang **Copy Editor:** Ting-Ting Hu **Production Editor:** Ting-Ting Hu

## Abstract

The preparation of subnanometric non-noble metal catalyst remains difficult especially when the metal loading is more than 1 wt%. Herein, the subnanometric nickel clusters (0.87 nm) were fabricated over the Ni/SAPO-11 catalyst for n-hexane hydroisomerization with Ni loading of 1.8 wt%. They exhibit 3.4 times the content of Ni atoms on corner and step sites than nanoparticles. These special Ni atoms with rich dangling bonds and high surface energy exhibit enhanced ability in activation and breakage of the C–H in n-hexane and H–H bonds in H<sub>2</sub>. Density functional theory results confirm that the activation energy for n-hexane dehydrogenation over Ni atoms on corner or step sites is only 10% and 60% of the one on terrace sites. The projected d-electron density states calculations reveal that the molecular-like electronic state of the nickel clusters is further strengthened when reducing the size to subnanometric level. It leads to the upshifting of the d-band center, which favors the activation of C–H and H–H bonds. All of these geometric and electronic effects generated by the subnanometric Ni clusters endow the Ni/SAPO-11 catalyst with 2.3 times the rate of i-C<sub>6</sub> generation and nearly 2.8 times the turnover frequency of its nanoparticle counterpart.

**Keywords:** Subnanometric Ni clusters, Ni/SAPO-11 catalyst, hydroisomerization geometric, electronic effects



© The Author(s) 2025. **Open Access** This article is licensed under a Creative Commons Attribution 4.0 International License (<https://creativecommons.org/licenses/by/4.0/>), which permits unrestricted use, sharing, adaptation, distribution and reproduction in any medium or format, for any purpose, even commercially, as long as you give appropriate credit to the original author(s) and the source, provide a link to the Creative Commons license, and indicate if changes were made.



## INTRODUCTION

The metal supported catalysts are popular in energy conversion and management<sup>[1-3]</sup>, and developing new efficient catalysts is of great significance to promote lower-carbon utilization processes and environmental protection. As an important application field of supported metal catalysts, hydroisomerization of alkanes plays a significant role in improving the low-temperature fluidity of bio-fuels such as biodiesel and producing high-octane clean gasoline, and thus promises to relieve energy crisis and environmental problems<sup>[4,5]</sup>. The catalysts used in this process show pronounced activity and selectivity dependence on metal particle size. It is well acknowledged that downsizing the metal particles increases the exposure rate and accessibility of the active atoms. Moreover, the metal species exhibit a molecular-like electronic structure and unique geometric structure when their particle size is reduced to a subnanometric level<sup>[6-10]</sup>. This usually imparts distinct activity and selectivity to the catalyst compared to the nanoparticle or single-atom counterpart<sup>[11-13]</sup>.

Geometrically, subnanometric metal clusters expose more atoms located at the corner and edge sites than nanoparticles<sup>[6]</sup>. These coordinatively unsaturated atoms usually exhibit distinct behavior in chemical bond breaking and formation in catalytic reactions<sup>[14-16]</sup>. At the electronic level, quantum size effects caused by the subnanometric clusters also significantly change the energy levels and then influence the orbital hybridization and overall charge transfer between metal and reactants or supports<sup>[17,18]</sup>. The combination of the above-mentioned geometric and electronic effects of the subnanometric clusters usually endows the catalyst with distinguished catalytic performance from the nanoparticle catalyst. For instance, the subnanometric Pt clusters show a turnover frequency (TOF) 40-100 times higher than their nanoparticle counterparts in oxidative dehydrogenation of propane. Such a high activity results from the enhanced ability in activation and breaking of C-H in propane over the under-coordinated Pt atoms on the surface of the Pt clusters<sup>[19]</sup>. A similar phenomenon was observed for the Ru/Al<sub>2</sub>O<sub>3</sub> catalyst for reduction of CO<sub>2</sub><sup>[18]</sup>. The electron transfer between the Al<sub>2</sub>O<sub>3</sub> and subnanometric Ru clusters was largely enhanced compared to Ru nanoparticles. The former exhibited lower CO<sub>2</sub> activation energy and CO formation energy, showing a CO selectivity 1.5 times higher than the latter. Yang *et al.* also observed the size-dependent electronic and geometric effects of the Pt clusters over the Pt/graphene catalyst for ammonia borane hydrolysis<sup>[20]</sup>. They found that the Pt dimers with the C-Pt-Pt-O structure were the active sites that exhibit higher catalytic activity than the single atoms and nanoparticles. In the catalytic reduction of NO with CO, Estefania also found that the subnanometric Pt clusters with a particle size of 0.2-0.7 nm exhibited higher activity in NO dissociation and CO oxidation at low temperatures due to its molecular-like electronic and unique geometric structures<sup>[21]</sup>.

As previously reported, only a change of one atom may cause apparent variation of the geometric and electronic properties of the subnanometric clusters<sup>[22-24]</sup>. It makes the fundamental studies on the geometric and electronic effect of the subnanometric catalyst for different applications valuable. The hydroisomerization catalyst is a classical bifunctional catalyst composed of metal components for (de)hydrogenation and acid supports for isomerization. Increasing the metal dispersion can not only enhance the function of (de)hydrogenation, but also improve the synergy between acid and metal sites, increasing the activity and isomer selectivity<sup>[11,25]</sup>. However, study on the unique geometric and electronic effect of the subnanometric metal clusters, especially the non-noble metal clusters catalyst with higher metal loading is scarce, which may be attributed to the complex and challenging synthesis method. However, anyhow, this is an unfavorable situation for improving the catalytic activity of the hydroisomerization catalyst.

Herein, the Ni/SAPO-11 catalyst with subnanometric nickel clusters was fabricated via a facile method. The geometric and electronic effects caused by the subnanometric Ni clusters in activation of C–H bonds in n-hexane and H–H in H<sub>2</sub> were discussed systematically via characterizations and density functional theory (DFT) calculations. Finally, a highly efficient Ni-based catalyst was obtained for hydroisomerization of n-hexane. Therefore, this work opens the application of subnanometric Ni clusters in alkanes hydroisomerization and contributes to improvements of the basic catalysis theory of subnanometric metal clusters in this reaction.

## EXPERIMENTAL

### Chemicals

Pseudo-boehmite with a solid content of 70 wt% was supplied by Yantai Henghui Petrochemical Co., Ltd. Phosphoric acid was from XiRong Petrochemical Co., Ltd. The dipropylamine (DPA, 99.0 wt% C<sub>6</sub>H<sub>15</sub>N), Ni(NO<sub>3</sub>)<sub>2</sub>·6H<sub>2</sub>O and nickel acetylacetonate (C<sub>10</sub>H<sub>14</sub>NiO<sub>4</sub>) were obtained from Aladdin Chemical Co., Ltd. Silica sol (SiO<sub>2</sub> 30.0 wt%) was provided by Qingdao Haiyang Petrochemical Co., Ltd. All the materials used in the experiments without further treatment.

### Catalysts synthesis

Firstly, 4.34 g of pseudoboehmite was mixed into 27 g of deionized water. Then, 6.9 g of phosphoric acid and 3.3 g of DPA were added to the mixed solution in sequence. After that, the acidic silica sol was mixed into the mixture, followed by introduction of 0.75 g of nickel acetylacetonate. The mixed solution was placed in a water bath at 353 K, stirred and then evaporated to dryness. The above sample was transferred into a quartz bottle and placed into an autoclave which is heated at 473 K. Then, the solid was filtered, washed and dried at 383 K, and subsequently calcined at 773 K. The Ni content in the catalyst measured by inductively coupled plasma (ICP) was 1.8 wt%, and the catalyst was named 1.8%Ni/SAG-11.

In comparison, the catalysts with 1.8 wt% and 4 wt% Ni loading were prepared with the impregnation method which are named 1.8%Ni/SAM-11 and 4%Ni/SAM-11, respectively. The SAPO-11 used in this catalyst was prepared via the same procedure as 1.8%Ni/SAG-11 but without nickel introduction.

### Characterization

Phase structure of the catalysts was tested on PANalytical B.V. Netherlands X-ray diffraction (XRD). X-ray photoelectron spectroscopy (XPS) was measured by Thermo Fisher Escalab with Al K $\alpha$  radiation. The morphological characterizations of the catalysts were performed by emission scanning electron microscopy (SEM) (JEOL, JSM-7900F) and transmission electron microscopy (TEM) measurements were conducted on the TEM (FEI Titan G2 80-200). The hydrogen chemisorption [hydrogen temperature-programmed desorption (H<sub>2</sub>-TPD)] was carried out on the Micromeritics 2920 chemisorption analyzer to analyze the surface Ni atoms. The temperature-programmed reduction of hydrogen (H<sub>2</sub>-TPR) was also conducted on the same instrument. The infrared spectra of the catalysts or catalysts adsorbed with pyridine were measured by a Nicolet-6700 Fourier transform infrared (FTIR) spectrometer. The CO-adsorbed FTIR measurements were carried out in the in-situ cell until at 10<sup>-2</sup> Pa and 133 K. The n-hexane-adsorbed FTIR was carried out after desorption in vacuum at different temperatures (323–398 K).

### Catalytic performance

The activity and selectivity of the catalysts in n-hexane hydroisomerization were measured in a fixed bed reactor. The catalyst was reduced by hydrogen at 823 K for 2 h. Then, the n-hexane was pumped into the reactor and the reaction was performed at 2 MPa with a weight hourly space velocity (WHSV) of 1.0 h<sup>-1</sup>. The molar ratio of H<sub>2</sub> to n-hexane is 4.0.

The TOF of metal sites (labeled as  $\text{TOF}_{\text{n-C}_6}$ ) was calculated according to

$$\text{TOF}_{\text{n-C}_6} = \frac{C_f * V * X}{W_{\text{Ni}} * C_{\text{Ni}}} (\text{h}^{-1})$$

where  $C_f$  is the concentration of n-hexane species ( $\text{mol} \cdot \text{mL}^{-1}$ ),  $v$  is the flow rate ( $\text{mL} \cdot \text{h}^{-1}$ ),  $X$  is the n-hexane conversion,  $W_{\text{Ni}}$  is the content of Ni in the catalyst (g), and  $C_{\text{Ni}}$  is the number of surface Ni atoms measured by hydrogen chemisorption.

## RESULTS AND DISCUSSION

### Fabrication of subnanometric Ni clusters over SAPO-11

The phase structure features of the catalysts are shown in Figure 1. All the catalysts show characteristic diffraction peaks of the AEL topology (2 Theta = 8.1°, 9.4°, 13.1°, 15.6° and 23.2°) [Figure 1A]. The peak intensity of the Ni/SAM-11 catalyst is obviously lower than that of SAPO-11, which is due to the structure destruction of SAPO-11 by the solvent<sup>[26,27]</sup>. The relative crystallinity of 1.8%Ni/SAG-11 increases significantly compared to the SAPO-11, implying that the addition of Ni promotes the crystallization of SAPO-11<sup>[28]</sup>. Both 1.8%Ni/SAM-11 and 4%Ni/SAM-11 show obvious Ni diffraction peaks (JCPDS 01-070-1849) [Figure 1B] due to the serious aggregation of Ni particles<sup>[29]</sup>. In contrast, the 1.8%Ni/SAG-11 catalyst shows no diffraction peaks of Ni, probably due to the uniform dispersion of Ni or the low Ni content below test limitation.

The  $\text{H}_2$ -TPR profiles of catalysts are demonstrated in Figure 2. The three  $\text{H}_2$  consumption peaks of the 1.8%Ni/SAM-11 and 4%Ni/SAM-11 are assigned to the reduction of NiO. Compared with 1.8%Ni/SAM-11 and 4%Ni/SAM-11, the 1.8%Ni/SAG-11 exhibits a higher reduction temperature due to the stronger metal-support interaction<sup>[30]</sup>. As for the 1.8%Ni/SAG-11 catalyst, peak I and peak II belong to reduction of NiO while peak III belongs to reduction of  $\text{NiAl}_2\text{O}_4$ <sup>[31]</sup>. The results suggest that the Ni/SAPO-11 prepared with the *in-situ* synthesis method exhibits stronger interaction between NiO and SAPO-11 compared with the counterpart prepared with impregnation method. The stronger metal-support interaction can inhibit metal agglomeration during high-temperature reduction, and this will be proved by the TEM images.

TEM was used to explore the particle size distribution of Ni of the catalysts, and the results are illustrated in Figure 3. The dark spots in the TEM images represent metallic Ni particles. The Ni particles are heavily aggregated on the surface of the 4%Ni/SAM-11 and 1.8%Ni/SAM-11 with a mean size of 26 and 20 nm, respectively. In contrast, subnanometric nickel clusters with an average size of 0.87 nm are observed over the 1.8%Ni/SAG-11. It can also be confirmed by the high-resolution TEM (HR-TEM) and high-angle annular dark-field scanning TEM (HAADF-STEM) images in Supplementary Figures 1 and 2, and Figure 4. Figure 3A shows schemes of the formation of subnanometric Ni clusters over the SAPO-11. The special barrier effect and protective effect of acetylacetonate ligands hinder aggregation of Ni during the thermal treatment process, leading to a high initial dispersion of NiO. Besides, the steric hindrance caused by the zeolite skeleton and pores, along with the strong metal-support interaction, also suppresses the aggregation of Ni. All of these factors contribute to the formation of subnanometric Ni clusters over the Ni/SAPO-11 catalyst.

The XPS spectra in the Ni 2p region of the reduced catalysts are shown in Figure 5. For the 1.8%Ni/SAM-11 and 4%Ni/SAM-11, the peaks at around 853.7 and 871 eV belong to the  $\text{Ni}^0$ <sup>[32,33]</sup>. Additional peaks around 857 and 874.3 eV on the spectrum of the catalysts indicate the existence of NiO<sup>[34]</sup>. The presence of NiO may be due to the exposure of the reduced catalysts to air during the sample transfer<sup>[35]</sup>. Apart from the peaks of  $\text{Ni}^0$  and NiO, there are new peaks at around 858 ( $\text{Ni}2\text{p}_{3/2}$ ) and 875.3 eV ( $\text{Ni}2\text{p}_{1/2}$ ) belonging to  $\text{Ni}^{2+}$  in  $\text{NiAl}_2\text{O}_4$

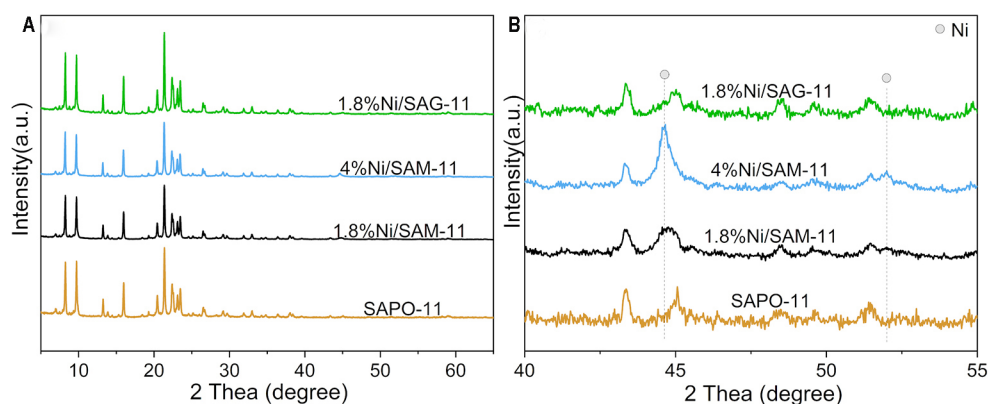


**Figure 1.** XRD patterns (A) and locally amplified one (B) of SAPO-11 and reduced Ni/SAPO-11 catalysts. XRD: X-ray diffraction.

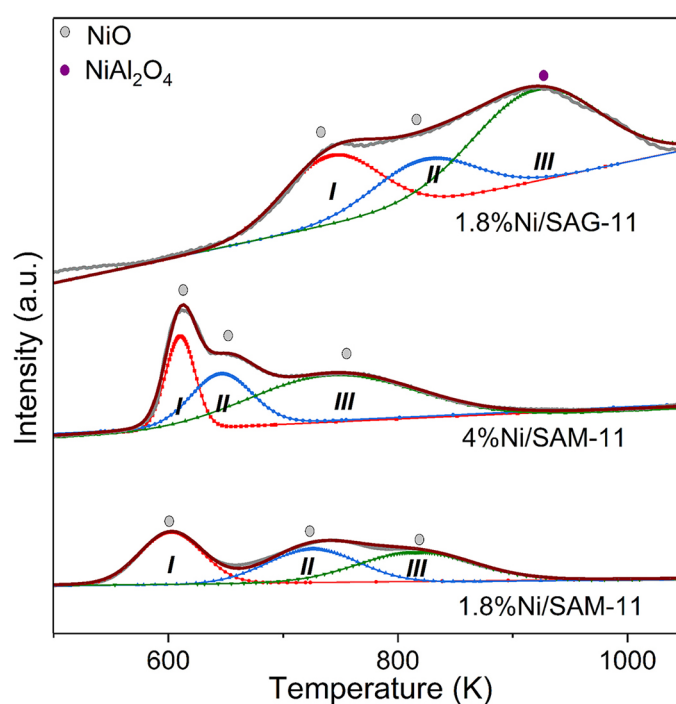


**Figure 2.** H<sub>2</sub>-TPR profiles of the Ni/SAPO-11 catalysts. H<sub>2</sub>-TPR: Temperature-programmed reduction of hydrogen.

over the 1.8%Ni/SAG-11<sup>[36]</sup>. The binding energy of metallic Ni over the 1.8%Ni/SAG-11 shifts to a higher value compared with the 1.8%Ni/SAM-11 and 4%Ni/SAM-11, which is probably caused by the different atomic relaxation of Ni with large or small particle size<sup>[6,37]</sup>.

### Geometric and electronic features of the subnanometric Ni clusters

The FTIR spectroscopy of the catalyst after CO adsorption was conducted to investigate the geometric effects caused by subnanometric Ni clusters [Figure 6A]. The peaks at 2,158 and 2,136 cm<sup>-1</sup> indicate presence of physical adsorption of CO<sup>[38]</sup>. The bands at 2,081 and 2,089 cm<sup>-1</sup> belong to the linear adsorption of CO on the edge and corner atoms of Ni, respectively<sup>[39–41]</sup>. In addition, 2,070 cm<sup>-1</sup> is assigned to linear absorption of CO on high-coordinated terraces of Ni<sup>[39–41]</sup>. The relative proportions of the peak areas at 2,088, 2,080 and 2,070 cm<sup>-1</sup> are shown in Supplementary Figure 3. The highest fraction of the corner and



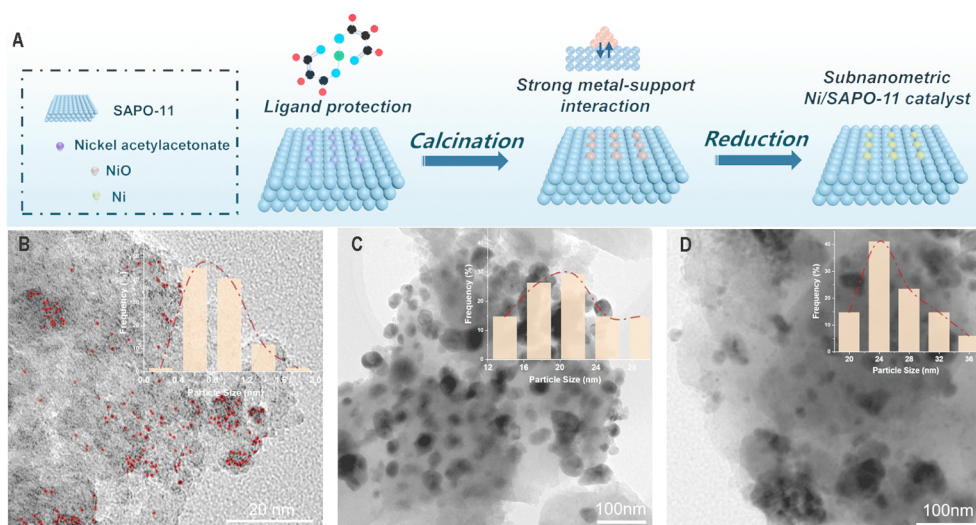


**Figure 3.** (A) Schematic illustration of sintering resistance over the 1.8%Ni/SAG-11 catalyst; TEM images of the reduced catalysts: (B) 1.8%Ni/SAG-11; (C) 1.8%Ni/SAM-11 and (D) 4%Ni/SAM-11. TEM: Transmission electron microscopy.

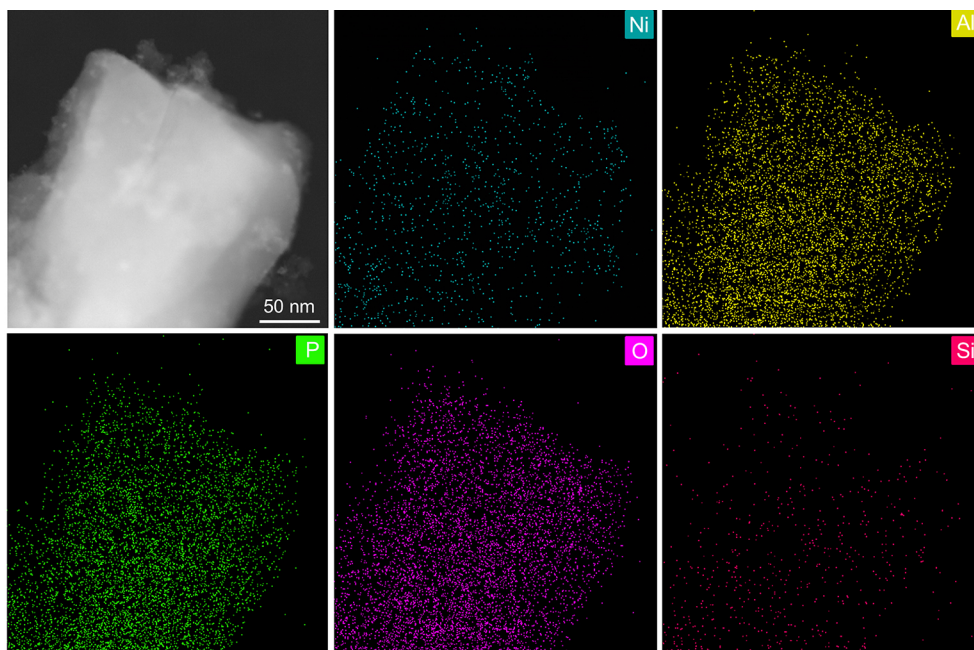


**Figure 4.** HAADF-STEM images of the reduced 1.8%Ni/SAG-11 and the corresponding STEM-mapping mapping images for Ni, Al, O, P, and Si elements. HAADF-STEM: High-angle annular dark-field scanning TEM; TEM: transmission electron microscopy.

edge Ni sites is observed over the subnanometric nickel clusters. The content of these Ni atoms increases by 2.4 times when the particle size of Ni decreases from ca. 26 to 0.87 nm. The results indicate that the subnanometric nickel clusters expose more corner and edge atoms than the nanoparticle counterpart.

The H<sub>2</sub>-TPD profiles of the Ni/SAPO-11 catalysts are demonstrated in Figure 6B. All the catalysts show a clear peak in the range of 350–500 K. Figure 6B indicates that the 1.8%Ni/SAG-11 has the strongest ability for adsorption of hydrogen, followed by the 4%Ni/SAM-11 and 1.8%Ni/SAM-11. The hydrogen desorption

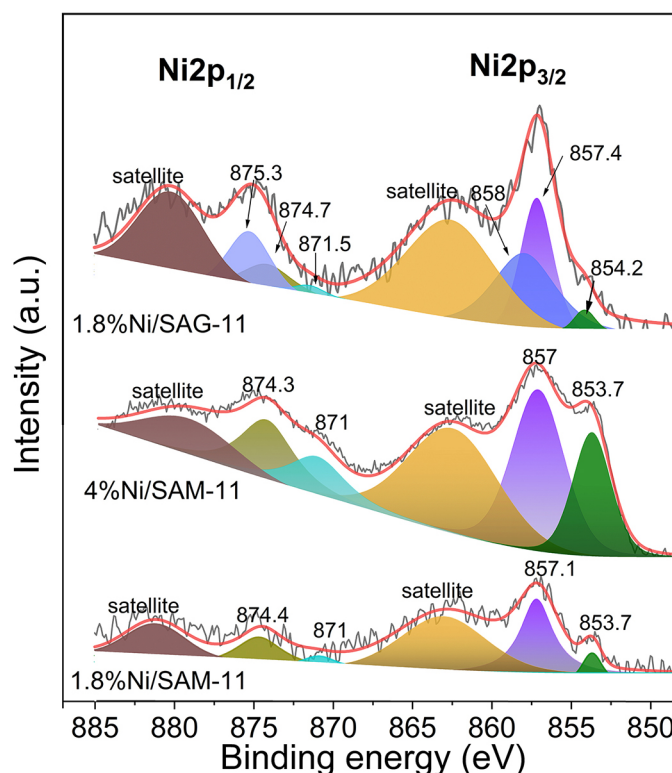


**Figure 5.** XPS spectra of the Ni 2p for the reduced catalysts. XPS: X-ray photoelectron spectroscopy.

temperature follows the same sequence, indicating the stronger hydrogen adsorption ability of the 1.8%Ni/SAG-11 catalyst. It is well acknowledged that the metal atoms on edge and corner sites are more unsaturated and show stronger hydrogen adsorption strength than the ones with a high-coordination number. That is because these surface atoms have more dangling bonds and higher surface energy, promoting adsorption and activation of H–H bonds<sup>[42,43]</sup>. The CO-adsorbed FTIR spectroscopy has confirmed the higher fraction of corner and edge Ni sites over the subnanometric metal clusters. Therefore, the subnanometric nickel clusters over the 1.8%Ni/SAG-11 show stronger ability to adsorb and activate H<sub>2</sub> than the nanoparticles.

DFT calculations were used to explore the reasons for the strong hydrogen adsorption and activation ability of the subnanometric nickel clusters over the 1.8%Ni/SAG-11 catalyst. The constructed models of nickel clusters are composed of 13, 55, 147 and 309 atoms, which are named Ni<sub>13</sub>, Ni<sub>55</sub>, Ni<sub>147</sub>, and Ni<sub>309</sub>, respectively [Supplementary Figure 4]. These models were used to study the difference in hydrogen adsorption ability between subnanometric nickel clusters [13 atoms (0.8 nm)] and nanometric nickel clusters [55 atoms (1.2 nm), 147 atoms (1.6 nm) and 309 atoms (2.1 nm)]. The H<sub>2</sub> atoms are mainly absorbed at low symmetry short bridge sites at the edges [Supplementary Figure 5]<sup>[17]</sup>. As shown in Figure 6C, the absorption energy of hydrogen on the (211) bridge sites increases with decreasing particle size. Particularly, it increases suddenly as the particle size of the Ni decreases to the subnanometric level. It indicates the significant enhancement in hydrogen adsorption and activation as the particle size of Ni decreases to the subnanometric scale.

The projected d-electron density of states (PDOS) calculations were used to provide electronic-level insights into the reasons for the sharply enhanced hydrogen adsorption ability of the subnanometric Ni clusters.

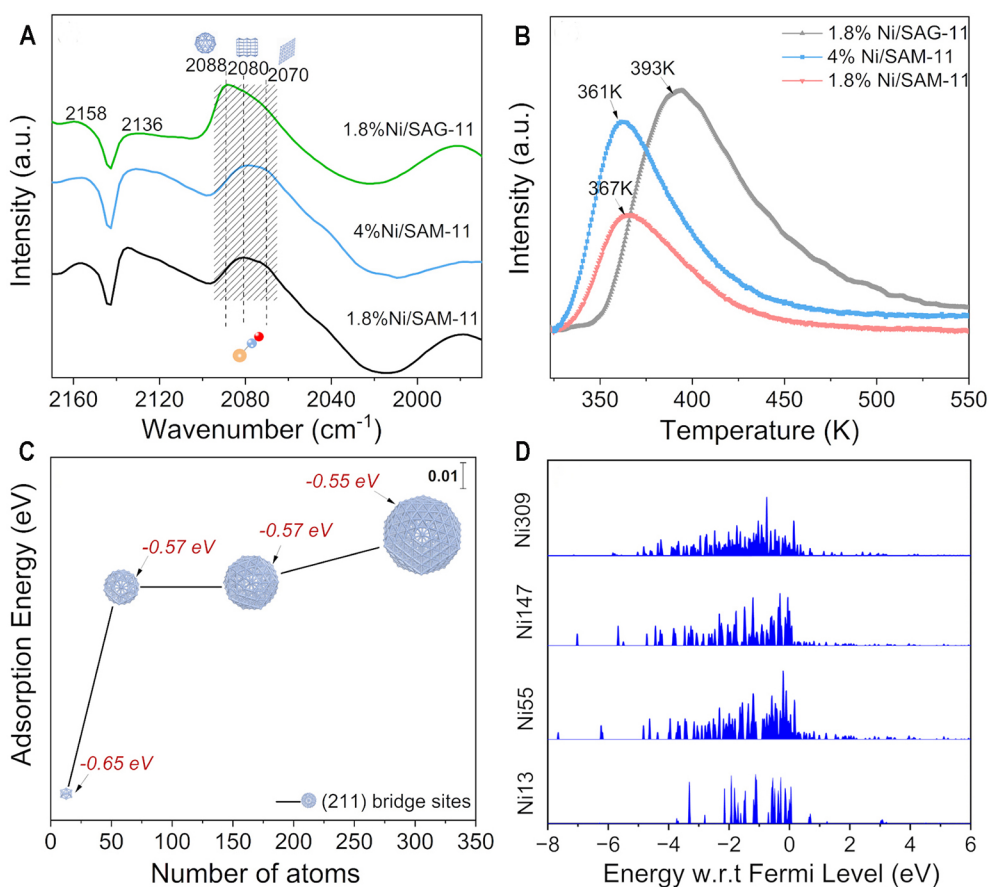


**Figure 6.** (A) CO-adsorbed FTIR spectroscopy and (B) H<sub>2</sub>-TPR profiles of the catalysts; (C) Calculated adsorption energies of H on the (211) bridge sites of Ni13, Ni55, Ni147 and Ni309 models; (D) Projected d-band density of states for Ni13, Ni55, Ni147 and Ni309 models. FTIR: Fourier transform infrared; H<sub>2</sub>-TPR: temperature-programmed reduction of hydrogen.

Figure 6D shows the projected d-band density of states for surface Ni atoms of the Ni13, Ni55, Ni147 and Ni309 models. A weak degree of energy level splitting between the atoms creates a narrower and more discrete d-band spectrum when decreasing the coordination number of the surface atoms. It is reported that the molecular-like d-electron state exhibits discrete d-band structures, while the metal-like d-electron state shows a continuous one<sup>[17]</sup>. For the subnanometric nickel cluster (13 atoms), the molecular-like d-electronic state with discrete d-band energy levels is observed, indicating that the unsaturation coordination of the corner and edge atoms over the metal cluster is further strengthened<sup>[44]</sup>. This leads to upshifting of the d-band center [Supplementary Table 1]. It thermodynamically favors the activation of H–H and C–H bonds<sup>[45,46]</sup>. As a result, subnanometric nickel clusters with upshifted d-band centers exhibit a stronger ability for the activation and absorption of hydrogen than nanoparticles.

To further analyze the interaction between n-hexane and nickel clusters, n-hexane-absorbed FTIR spectroscopy was conducted over the catalysts and the results are shown in Figure 7. The characteristic stretching vibrations of C–H bonds of CH<sub>3</sub> and CH<sub>2</sub> are in the region of 3,000–2,700 cm<sup>-1</sup><sup>[47,48]</sup>. In detail, 2,962 and 2,933 cm<sup>-1</sup> correspond to the antisymmetric stretching vibrations of C–H bonds. The bands at 2,873 and 2,862 cm<sup>-1</sup> belong to symmetric stretching vibration of the C–H bond. The redshift of the C–H stretching absorption bands over the 1.8%Ni/SAG-11 can be observed compared with the 1.8%Ni/SAM-11 and 4%Ni/SAM-11. The metal sites in the 1.8%Ni/SAG-11 are dominated by corner and edge atoms. These atoms have strong electron-withdrawing induction effects<sup>[19]</sup>, resulting in charge transfer from the n-hexane C–H bond



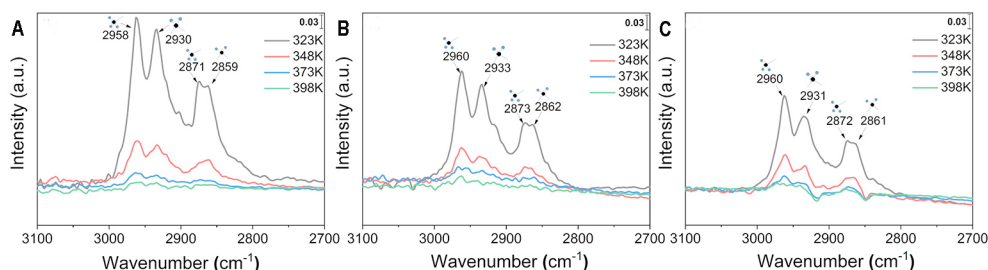


**Figure 7.** n-Hexane-absorbed FTIR spectroscopy of the reduced (A)1.8%Ni/SAG-11, (B)4%Ni/SAM-11 and (C)1.8%Ni/SAM-11. FTIR: Fourier transform infrared.

orbital to the nickel cluster. It weakens the C–H bonds and then the decrease in the vibration frequency of C–H bonds can be observed. Besides, Figure 7 also indicates that the saturated adsorption capacity of n-hexane decreases in the order of: 1.8%Ni/SAG-11 > 4%Ni/SAM-11 > 1.8%Ni/SAM-11. The 1.8%Ni/SAG-11 has the highest n-hexane adsorption capacity due to the highest number of surface metal atoms. Therefore, the Ni/SAPO-11 with subnanometric nickel clusters possesses a stronger n-hexane adsorption ability than the one with nickel nanoparticles.

DFT calculation was also used to explore the difference in n-hexane activation over the Ni atom at different locations. As shown in Supplementary Figure 6, flat Ni(111), stepped Ni(211) and cubic octahedron of the Ni cluster correspond to terrace, edge and corner sites of Ni, respectively. Figure 8 shows the energy required for C–H bond activation of n-hexane on corner, edge and terrace Ni atoms ( $C_6H_{14} \rightarrow C_6H_{12}^* + 2H^*$ ).  $E_{a1}$  represents the energy required for the first C–H bond activation ( $C_6H_{14} \rightarrow C_6H_{13}^* + H^*$ ), while  $E_{a2}$  represents the energy required for the second C–H bond activation ( $C_6H_{13} \rightarrow C_6H_{12}^* + H^*$ ). It is clear that the  $E_{a1}$  ( $E_{a1}$ ,  $E_{a2}$ ) values for the corner and edge atoms are relatively low. The computational activation energy for n-hexane dehydrogenation over terrace Ni atoms is ca. 1.1 and 1.6 times that on the edge and corner ones, respectively, supporting the n-hexane-absorbed FTIR results. The higher activation ability of the corner and edge sites is attributed to their special electronic features. The high proportion of the low-coordinated surface atoms leads to the upshifting of the d-band center, which thermodynamically favors the activation of C–H bonds<sup>[19,47]</sup>. The PDOS calculations mentioned above reveal that the unsaturation coordination of the subnanometric nickel cluster is further strengthened. Therefore, the 1.8%Ni/SAG-11 has the stronger activation ability of n-hexane.

### Catalytic performance

The hydroisomerization performance of the catalysts was tested with n-hexane as the model reactants. As shown in Figure 9 and Supplementary Table 2, the 1.8%Ni/SAG-11 exhibits the highest activity and isomer selectivity. Specifically, at 613 K, the 1.8%Ni/SAG-11 shows an isomer selectivity of 95.6% at the conversion of 70.3% which is significantly higher than the corresponding values of the 1.8%Ni/SAM-11 (73.2%, 25.6%) and 4%Ni/SAM-11 (81.3%, 50.1%) catalysts [Figure 9B and Supplementary Figure 7]. It is found that the n-hexane conversion and i-C<sub>6</sub> yield are 70.3% and 67.2%, respectively, which are comparable to those of the Pt/SAPO-11 catalyst (72.8% and 67.1%) at the same reaction condition (613 K, 2.0 MPa, H<sub>2</sub>/n-C<sub>6</sub> = 4.0 and WHSV = 1.0 h<sup>-1</sup>), and the detailed comparison of the two catalysts can be found in Supplementary Table 3. The i-C<sub>6</sub> formation rate over the 1.8%Ni/SAG-11 is much higher than the 1.8%Ni/SAM-11 and 4%Ni/SAM-11 at the same reaction temperature, which confirms the higher activity and selectivity of the 1.8%Ni/SAG-11 catalyst.

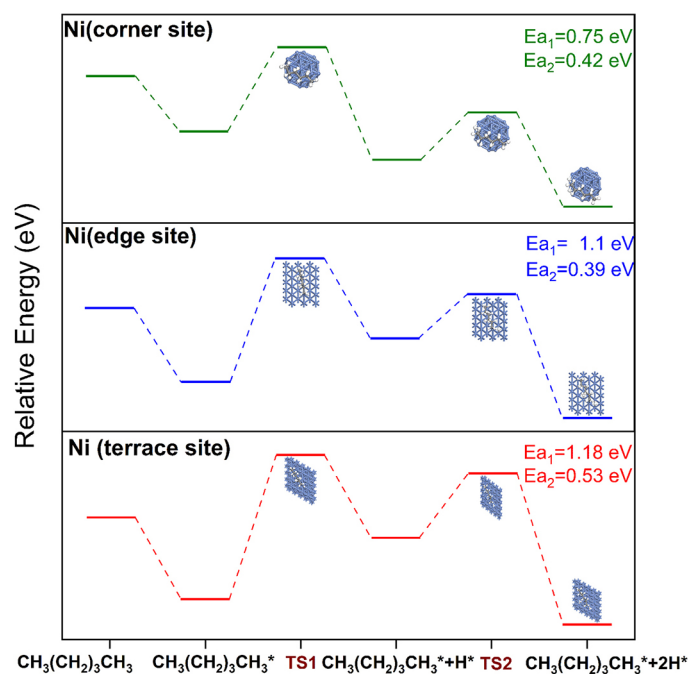


**Figure 8.** Potential energy profiles for the activation of n-hexane ( $\text{C}_6\text{H}_{14} \rightarrow \text{C}_6\text{H}_{12} + 2\text{H}^\cdot$ ) on corner, edge and terrace Ni atom, respectively.

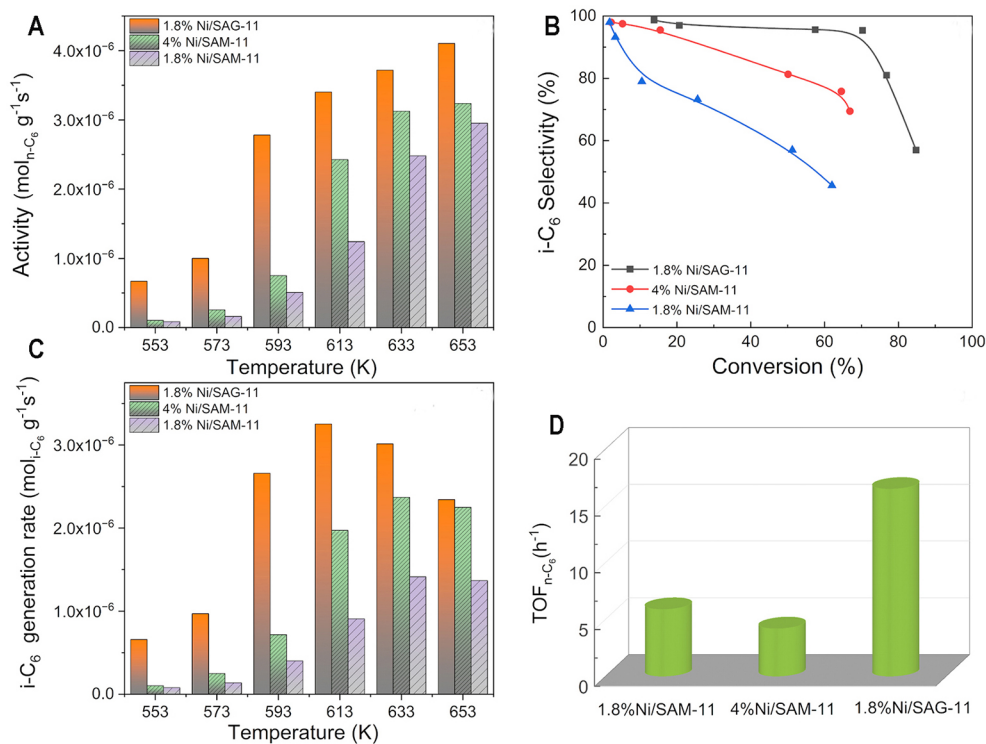


**Figure 9.** (A) Activity (n-hexane converted per gram of catalyst per second); (B) i-C<sub>6</sub> selectivity; (C) i-C<sub>6</sub> generation rate and (D) TOF<sub>n-C<sub>6</sub></sub> of the catalysts at 553 K in n-hexane hydroisomerization. TOF: Turnover frequency.

The hydroisomerization of alkanes undergoes three sequential steps: (i) alkane dehydrogenation on metal sites to form alkenes; (ii) skeletal rearrangement of the alkenes on acid sites; (iii) hydrogenation of iso-alkenes to iso-alkanes on metal sites<sup>[7]</sup>. According to the pyridine adsorption infrared spectroscopy (Py-IR) results [Supplementary Figure 8 and Supplementary Table 4], the content of Brønsted acid sites of 1.8%Ni/SAG-11 is only slightly higher than that of 1.8%Ni/SAM-11 and 4%Ni/SAM-11 catalysts. Therefore, the hydroisomerization performance of the catalyst mainly depends on the number and geometric and electronic features of metal sites. The subnanometric Ni clusters over the 1.8%Ni/SAG-11 provide more metal sites for (de)hydrogenation reaction than those of the other two catalysts.

The TOF was calculated with n-hexane conversion lower than 15% [Supplementary Table 5] and exclusion of the internal and external diffusion effect [Supplementary Tables 6 and 7]. The intrinsic activity of the Ni atom in subnanometric nickel clusters is increased greatly compared with that in the nanoparticles. As shown in Figure 9D and Supplementary Table 8, the  $\text{TOF}_{\text{n-C}_6}$  over the 1.8%Ni/SAG-11 catalyst is about 2.8 times higher than that over the 4%Ni/SAM-11 catalyst. Such a high  $\text{TOF}_{\text{n-C}_6}$  over the 1.8%Ni/SAG-11 is attributed to the large number of low-coordinated Ni atoms in the subnanometric Ni clusters which possess significantly enhanced ability in activation of C–H and H–H bonds. Besides, the coordination unsaturation and molecular-like electronic state of the nickel clusters are significantly enhanced as the metal size decreases to the subnanometric level. This causes the upshifting of the d-band center which further strengthens the ability in activation of n-hexane and  $\text{H}_2$  of nickel clusters. Sufficient metal sites and highly active corner and edge Ni sites make the formed hexene intermediates be hydrogenated timely before their cracking, increasing the isomer selectivity. Therefore, the 1.8%Ni/SAG-11 with subnanometric Ni clusters exhibits significantly higher activity and selectivity than the nanoparticle counterpart in n-hexane hydroisomerization.

Figure 10 presents the ratio of dimethylbutane to methyl pentane selectivity (DMB/MP) and cracking product to iso-hexane selectivity (C/I) as a function of n-hexane conversion. For the 1.8%Ni/SAM-11 and 4%Ni/SAM-11 catalysts, the DMB/MP ratio is not zero at near-zero conversion. The DMB/MP and C/I ratios increase sharply with conversion. The results indicate that both MP and DMB are primary products over the 1.8%Ni/SAM-11 and 4%Ni/SAM-11 catalysts. This was due to its insufficient metal sites, and thus the reaction intermediates are prone to secondary skeletal isomerization and even cracking at the acid sites. It can be deduced that these catalysts follow the reaction path of  $\text{n-C}_6 \rightleftharpoons \text{DMB} + \text{MP} \rightarrow \text{C}$ . For the 1.8% Ni/SAG-11 catalyst, the DMB/MP and C/I ratios tend to be zero at near-zero conversion, and the two ratios show no significant increase below 70% n-hexane conversion. The results confirm sufficient metal sites and a high proportion of edge and corner Ni atoms over the 1.8%Ni/SAG-11 catalyst which guarantees the timely hydrogenation of intermediates and avoids excessive skeletal rearrangement at the acid sites. Under such circumstances, only MP behaves as the primary product. Only when high hexane conversion is reached are DMB and cracking products generated by MP in sequence, following the reaction path:  $\text{n-C}_6 \rightleftharpoons \text{MP} \rightleftharpoons \text{DMB} \rightarrow \text{C}$ . Therefore, 1.8% Ni/SAG-11 presents higher selectivity and i-C<sub>6</sub> generation rate.

## CONCLUSIONS

The subnanometric Ni clusters with a mean size of 0.87 nm were successfully fabricated over the Ni/SAPO-11 hydroisomerization catalyst. Such small metal clusters exhibit pronounced geometric and electronic effects in this reaction. The decrease of Ni particle size from ca. 26 to 0.87 nm increases the content of corner and edge Ni atoms by 2.4 times. These Ni atoms with low-coordination numbers are more active in adsorption and activation of C–H bonds in n-hexane and H–H bonds in  $\text{H}_2$ . The computational activation energy for n-hexane dehydrogenation over terrace Ni atom is ca. 1.1 and 1.6 times that on the edge and corner ones, respectively. Besides, the coordination unsaturation of these Ni atoms is further enhanced for the subnanometric clusters. The subnanometric Ni clusters show a narrower and more discrete d-band

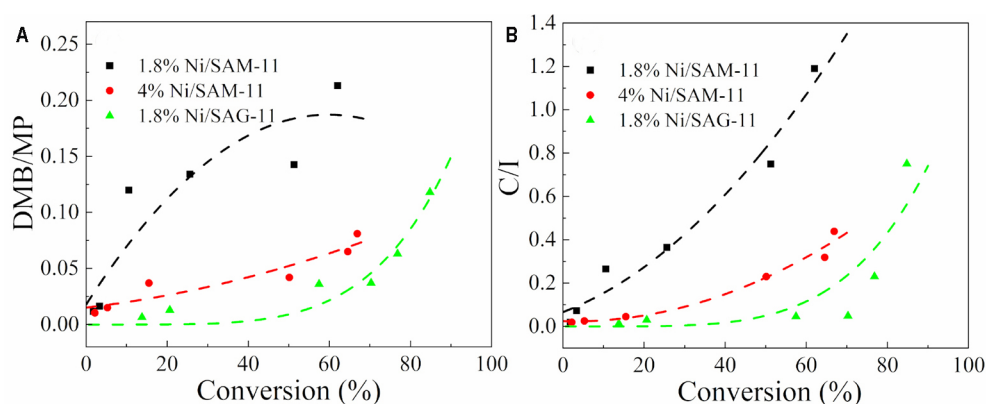


**Figure 10.** The product distribution of (A) DMB/MP and (B) C/I ratios as a function of  $n\text{-C}_6$  conversions in  $n\text{-hexane}$  hydroisomerization. DMB/MP: Dimethylbutane to methyl pentane selectivity.

spectrum. It leads to the upshifting of the d-band center which further improves the adsorption and activation of C–H and H–H bonds. The geometric and electronic characteristics of the subnanometric nickel cluster endow the Ni/SAPO-11 catalyst with superior catalytic performance to the nanoparticle counterpart in  $n\text{-hexane}$  hydroisomerization. The former shows an  $i\text{-hexane}$  formation rate of  $2.55\text{e-}6\text{ mol}\cdot\text{g}^{-1}\cdot\text{s}^{-1}$  and a  $\text{TOF}_{n\text{-C}_6}$  of  $16.5\text{ h}^{-1}$ , which are 3.6 times and nearly 2.8 times that of the latter, respectively.

## DECLARATIONS

### Authors' contributions

Supervision, writing - original draft, funding acquisition: Lyu, Y.

Investigation, writing - original draft: Fan, L.

Investigation: Gao, Y.

Investigation, software: Zhao, L.

Resources: Zhang, W.

Writing - review and editing: Li, F.

Methodology: Fu, J.

Supervision, conceptualization, funding acquisition: Liu, X.

### Availability of data and materials

The authors confirm that the data supporting the findings of this study are available within its [Supplementary Materials](#).

### Financial support and sponsorship

This work was supported by the National Natural Science Foundation of China (Grant Nos. 22108308, 22378427, 21991091), the Natural Science Foundation for Innovation and Development Joint Funds of Shandong Province (ZR2022LFG003), National Key Laboratory of Fluorinated Functional Membrane Materials, Natural Science Foundation of Shandong Province (ZR2024MB149), the Shandong Energy Institute (SEI) (Grant: SEI U202316), the National Key Research and Development Program of China (2022YFE0203400), the Taishan Scholar Youth Program of Shandong Province (tsqn202312118, tsqn202312114), and the Fundamental Research Funds for the Central Universities (23CX10005A).

### Conflicts of interest

All authors declared that there are no conflicts of interest.

**Ethical approval and consent to participate**

Not applicable.

**Consent for publication**

Not applicable.

**Copyright**

© The Author(s) 2025.

**REFERENCES**

1. Seufitelli, G. V.; Park, J. J.; Tran, P. N.; Dichiaro, A.; Resende, F. L.; Gustafson, R. Kinetics of ethylene oligomerization over Ni-H-Beta catalysts. *J. Catal.* **2021**, *401*, 40-53. DOI
2. Tang, X.; Wu, Y.; Fang, Z.; et al. Syntheses, catalytic performances and DFT investigations: a recent review of copper-based catalysts of methanol steam reforming for hydrogen production. *Energy* **2024**, *295*, 131091. DOI
3. Wang, S.; Cao, M.; Sun, S.; et al. Selective hydroisomerization of isobutane to n-butane over WO<sub>3</sub>-ZrO<sub>2</sub> supported Ni-Cu alloy. *Fuel* **2020**, *280*, 118274. DOI
4. Tang, R.; Zhang, J.; Shen, Z.; Li, T.; Luo, J.; Yang, T. Isomerization performance of n-hexane in hydrogen atmosphere over the multistage porous composite Ni<sub>x</sub>P<sub>y</sub>-MCM-41/MOR catalyst. *J. Energy. Inst.* **2024**, *114*, 101652. DOI
5. Morávková, J.; Pilař, R.; Bortnovsky, O.; et al. The effect of the nanoscale intimacy of platinum and acid centres on the hydroisomerization of short-chain alkanes. *Appl. Catal. A. Gen.* **2022**, *634*, 118535. DOI
6. Ma, L.; Yan, L.; Lu, A.; Ding, Y. Effects of Ni particle size on amination of monoethanolamine over Ni-Re/SiO<sub>2</sub> catalysts. *Chin. J. Catal.* **2019**, *40*, 567-79. DOI
7. Lyu, Y.; Yu, Z.; Yang, Y.; et al. Metal-acid balance in the in-situ solid synthesized Ni/SAPO-11 catalyst for n-hexane hydroisomerization. *Fuel* **2019**, *243*, 398-405. DOI
8. Chen, J.; Zhong, J.; Wu, Y.; et al. Particle size effects in stoichiometric methane combustion: structure-activity relationship of Pd catalyst supported on gamma-alumina. *ACS. Catal.* **2020**, *10*, 10339-49. DOI
9. Ostgard, D. The mechanism of hydrogenolysis and isomerization of oxacycloalkanes on metals IX. structure sensitive hydrogenolysis and isomerization of methyloxirane over well-characterized Pt/SiO<sub>2</sub> Catalysts\*1. *J. Catal.* **1991**, *129*, 519-23. DOI
10. Ebadi, H. Tracking of azobenzene isomerization by X-ray emission spectroscopy. *J. Phys. Chem. A* **2014**, *118*, 7832-7. DOI
11. Liu, L.; Corma, A. Metal catalysts for heterogeneous catalysis: from single atoms to nanoclusters and nanoparticles. *Chem. Rev.* **2018**, *118*, 4981-5079. DOI PubMed PMC
12. Baudouin, D.; Rodemerck, U.; Krumeich, F.; et al. Particle size effect in the low temperature reforming of methane by carbon dioxide on silica-supported Ni nanoparticles. *J. Catal.* **2013**, *297*, 27-34. DOI
13. Roduner, E. Size matters: why nanomaterials are different. *Chem. Soc. Rev.* **2006**, *35*, 583. DOI
14. Calle-vallejo, F.; Loffreda, D.; Koper, M. T. M.; Sautet, P. Introducing structural sensitivity into adsorption-energy scaling relations by means of coordination numbers. *Nature. Chem.* **2015**, *7*, 403-10. DOI
15. Cao, S.; Tao, F.; Tang, Y.; Li, Y.; Yu, J. Size- and shape-dependent catalytic performances of oxidation and reduction reactions on nanocatalysts. *Chem. Soc. Rev.* **2016**, *45*, 4747-65. DOI
16. Reske, R.; Mistry, H.; Beharfarid, F.; Roldan, C. B.; Strasser, P. Particle size effects in the catalytic electroreduction of CO<sub>2</sub> on Cu nanoparticles. *J. Am. Chem. Soc.* **2014**, *136*, 6978-86. DOI PubMed
17. Li, L.; Larsen, A. H.; Romero, N. A.; et al. Investigation of catalytic finite-size-effects of platinum metal clusters. *J. Phys. Chem. Lett.* **2013**, *4*, 222-6. DOI
18. Yan, Y.; Wang, Q.; Jiang, C.; et al. Ru/Al<sub>2</sub>O<sub>3</sub> catalyzed CO<sub>2</sub> hydrogenation: oxygen-exchange on metal-support interfaces. *J. Catal.* **2018**, *367*, 194-205. DOI
19. Vajda, S.; Pellin, M. J.; Greeley, J. P.; et al. Subnanometre platinum clusters as highly active and selective catalysts for the oxidative dehydrogenation of propane. *Nat. Mater.* **2009**, *8*, 213-6. DOI PubMed
20. Yang, J.; Fu, W.; Chen, C.; et al. Atomic design and fine-tuning of subnanometric Pt catalysts to tame hydrogen generation. *ACS. Catal.* **2021**, *11*, 4146-56. DOI
21. Fernández, E.; Liu, L.; Boronat, M.; Arenal, R.; Concepcion, P.; Corma, A. Low-temperature catalytic NO reduction with CO by subnanometric Pt clusters. *ACS. Catal.* **2019**, *9*, 11530-41. DOI PubMed PMC
22. Du, Y.; Sheng, H.; Astruc, D.; Zhu, M. Atomically precise noble metal nanoclusters as efficient catalysts: a bridge between structure and properties. *Chem. Rev.* **2020**, *120*, 526-622. DOI
23. Guo, X.; Gu, J.; Lin, S.; Zhang, S.; Chen, Z.; Huang, S. Tackling the activity and selectivity challenges of electrocatalysts toward the nitrogen reduction reaction via atomically dispersed biatom catalysts. *J. Am. Chem. Soc.* **2020**, *142*, 5709-21. DOI PubMed
24. Pan, Y.; Zhang, C.; Liu, Z.; Chen, C.; Li, Y. Structural regulation with atomic-level precision: from single-atomic site to diatomic and atomic interface catalysis. *Matter* **2020**, *2*, 78-110. DOI
25. Fan, L.; Zhao, L.; Lv, Y.; et al. Ionic liquid and lysine co-assisted synthesis of the highly dispersed Ni/SAPO-11 catalyst. *Inorg. Chem.*



- Front. 2022, 9, 3679-91. DOI
26. Simonot-grange, M.; Waldeck, A.; Barthomeuf, D.; Weber, G. Contribution to the study of framework modification of SAPO-34 and SAPO-37 upon water adsorption by thermogravimetry. *Thermochimica. Acta.* **1999**, 329, 77-82. DOI
  27. Briend, M.; Vomscheid, R.; Peltre, M. J.; Man, P. P.; Barthomeuf, D. Influence of the choice of the template on the short- and long-term stability of SAPO-34 zeolite. *J. Phys. Chem.* **1995**, 99, 8270-6. DOI
  28. Yu, G.; Chen, X.; Xue, W.; et al. Melting-assisted solvent-free synthesis of SAPO-11 for improving the hydroisomerization performance of n-dodecane. *Chin. J. Catal.* **2020**, 41, 622-30. DOI
  29. Liu, Q.; Gu, F.; Lu, X.; et al. Enhanced catalytic performances of Ni/Al<sub>2</sub>O<sub>3</sub> catalyst via addition of V<sub>2</sub>O<sub>5</sub> for CO methanation. *Appl. Catal. A. Gen.* **2014**, 488, 37-47. DOI
  30. Gil, A.; Diaz, A.; Gandía, L.; Montes, M. Influence of the preparation method and the nature of the support on the stability of nickel catalysts. *Appl. Catal. A. Gen.* **1994**, 109, 167-79. DOI
  31. Zhan, W.; Lyu, Y.; Liu, X.; Fan, L.; Li, F.; Yang, Y. The direct synthesis of Ni/SAPO-11 hydroisomerization catalyst via a novel two-step crystallization strategy. *Pet. Sci.* **2022**, 19, 2448-59. DOI
  32. Liu, Q.; Zhong, Z.; Gu, F.; et al. CO methanation on ordered mesoporous Ni-Cr-Al catalysts: effects of the catalyst structure and Cr promoter on the catalytic properties. *J. Catal.* **2016**, 337, 221-32. DOI
  33. Wang, T.; Zhang, W.; Li, Y.; et al. Quantitative synergy between metal and acid centers over the Ni/Beta bifunctional catalyst for methyl laurate hydrodeoxygenation to bio-jet fuel. *Fuel. Process. Technol.* **2023**, 241, 107602. DOI
  34. Wang, L.; Li, Z.; Zhang, P.; Wang, G.; Xie, G. Hydrogen generation from alkaline NaBH<sub>4</sub> solution using Co-Ni-Mo-P/ $\gamma$ -Al<sub>2</sub>O<sub>3</sub> catalysts. *Int. J. Hydrogen. Energy.* **2016**, 41, 1468-76. DOI
  35. Gao, J.; Jia, C.; Li, J.; et al. Ni/Al<sub>2</sub>O<sub>3</sub> catalysts for CO methanation: effect of Al<sub>2</sub>O<sub>3</sub> supports calcined at different temperatures. *J. Energy. Chem.* **2013**, 22, 919-27. DOI
  36. Kharat, A.; Pendleton, P.; Badalyan, A.; Abedini, M.; Amini, M. Decomposition of nickel formate on sol-gel alumina and characterization of product by X-ray photoelectron and TOF-SIMS spectroscopies. *J. Catal.* **2002**, 205, 7-15. DOI
  37. Liang, G.; Zhou, Y.; Zhao, J.; Khodakov, A. Y.; Ordonsky, V. V. Structure-sensitive and insensitive reactions in alcohol amination over nonsupported Ru nanoparticles. *ACS. Catal.* **2018**, 8, 11226-34. DOI
  38. Lee, Y.; Oyama, S. Bifunctional nature of a SiO<sub>2</sub>-supported Ni<sub>2</sub>P catalyst for hydrotreating: EXAFS and FTIR studies. *J. Catal.* **2006**, 239, 376-89. DOI
  39. Hu, C.; Chen, Y.; Li, P.; Min, H.; Chen, Y.; Tian, A. Temperature-programmed FT-IR study of the adsorption of CO and co-adsorption of CO and H<sub>2</sub> on NiAl<sub>2</sub>O<sub>3</sub>. *J. Mol. Catal. A.: Chem.* **1996**, 110, 163-9. DOI
  40. Poncelet, G.; Centeno, M.; Molina, R. Characterization of reduced  $\alpha$ -alumina-supported nickel catalysts by spectroscopic and chemisorption measurements. *Appl. Catal. A. Gen.* **2005**, 288, 232-42. DOI
  41. Råberg, L.; Jensen, M.; Olsbye, U.; et al. Propane dry reforming to synthesis gas over Ni-based catalysts: influence of support and operating parameters on catalyst activity and stability. *J. Catal.* **2007**, 249, 250-60. DOI
  42. Liu, B.; Lusk, M. T.; Ely, J. F. Influence of Nickel catalyst geometry on the dissociation barriers of H<sub>2</sub> and CH<sub>4</sub>: Ni<sub>13</sub> versus Ni(111). *J. Phys. Chem. C.* **2009**, 113, 13715-22. DOI
  43. Mårtensson, A.; Nyberg, C.; Andersson, S. Adsorption of hydrogen on a stepped nickel surface. *Surf. Sci.* **1988**, 205, 12-24. DOI
  44. Xiao, C.; Lu, B.; Xue, P.; et al. High-index-facet- and high-surface-energy nanocrystals of metals and metal oxides as highly efficient catalysts. *Joule* **2020**, 4, 2562-98. DOI
  45. Hu, Q.; Gao, K.; Wang, X.; et al. Subnanometric Ru clusters with upshifted D band center improve performance for alkaline hydrogen evolution reaction. *Nat. Commun.* **2022**, 13, 31660. DOI PubMed PMC
  46. Ru, W.; Liu, Y.; Fu, B.; Fu, F.; Feng, J.; Li, D. Control of local electronic structure of Pd single atom catalyst by adsorbate induction. *Small* **2022**, 18, e2103852. DOI PubMed
  47. Yang, X.; Li, Y.; Wang, Y.; Zheng, H.; Li, K.; Mao, H. Chemical transformations of n-hexane and cyclohexane under the upper mantle conditions. *Geosci. Front.* **2021**, 12, 1010-7. DOI
  48. Grahn, M.; Holmgren, A.; Hedlund, J. Adsorption of n-hexane and p-Xylene in thin silicalite-1 films studied by FTIR/ATR spectroscopy. *J. Phys. Chem. C.* **2008**, 112, 7717-24. DOI

**Yuchao Lyu**

Yuchao Lyu obtained his B.Sc. and Ph.D. degrees from China University of Petroleum in 2019. He is currently an associate professor at the College of Chemistry and Chemical Engineering in China University of Petroleum. His research focuses on the controllable synthesis and application of catalysts.

**Lei Fan**

Lei Fan obtained his Ph.D. degree under the supervision of Prof. Xinmei Liu.

**Yiming Gao**

Yiming Gao is an undergraduate student under the supervision of Yuchao Lyu.



**Lianming Zhao**

Lianming Zhao obtained his Ph.D. degree from China University of Petroleum. He is currently an associate professor at the School of Chemistry and Chemical Engineering of China University of Petroleum. His research focuses on new energy materials.



**Wenjing Zhang**

Wenjing Zhang is a master's degree candidate under the supervision of Prof. Xinmei Liu and Yuchao Lyu.



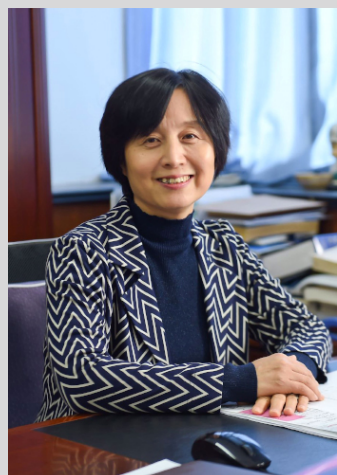
**Furang Li**

Furang Li is a Ph.D. student under the supervision of Prof. Xinmei Liu and Yuchao Lyu.



**Jianye Fu**

Jianye Fu received his Ph.D. degree in biomedical engineering from the University of Queensland in 2019. He is currently a researcher at China University of Petroleum. His research focuses on the design and synthesis of advanced functional materials.



**Xinmei Liu**

Xinmei Liu obtained her B.Sc. and Ph.D. degrees from China University of Petroleum. She is currently a professor at the College of Chemistry and Chemical Engineering of China University of Petroleum. Her research focuses on industrial catalysis and reactivation of spent catalysts.